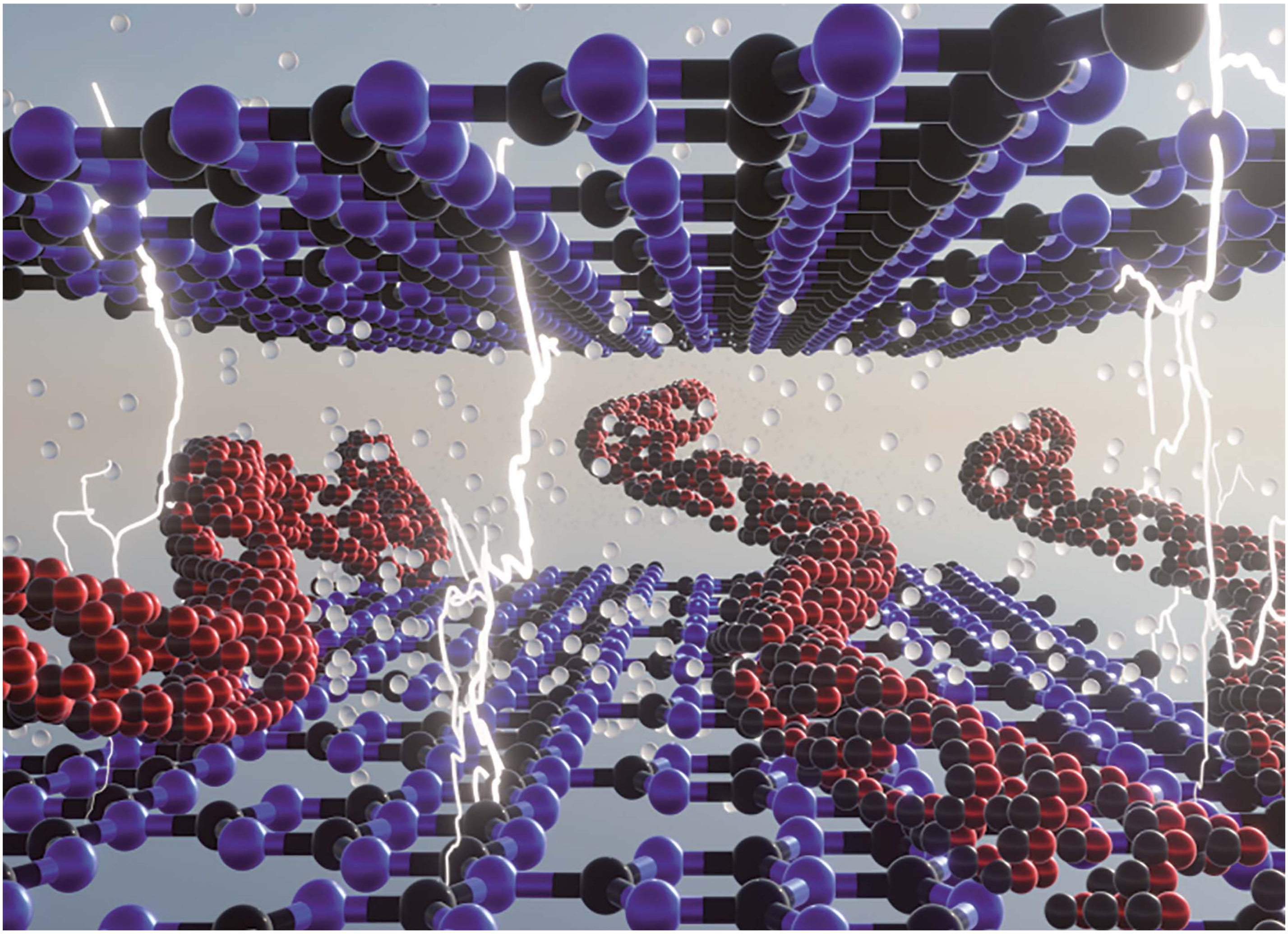

Showcasing research from Unité de Catalyse et Chimie du Solide (UCCS) and Institut d'électronique de microélectronique et de nanotechnologie (IEMN), Université de Lille, Lille, France.

Covalent organic framework derived synthesis of Ru embedded in carbon nitride for hydrogen and oxygen evolution reactions

We present an innovative approach for the synthesis of highly dispersed low-valence Ru oxide nanoparticles in the form of nanowires between carbon nitride layers using pyrolysis of 2D CIN-1 covalent organic framework (COF) material with embedded Ru(II) complexes. The resulting electrocatalyst demonstrates exceptional efficiency in water electrolysis with lower overpotentials for both hydrogen and oxygen production in comparison with Pt and RuO_2 reference catalysts, respectively.

As featured in:

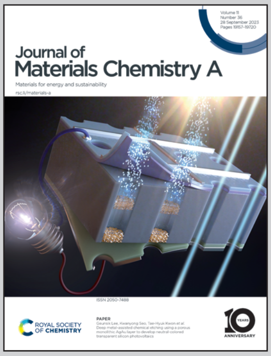

Volume 11
Number 36
28 September 2023
Pages 19157–19720

Journal of
Materials Chemistry A

Materials for energy and sustainability

rsc.li/materials-a

ISSN 2050-7488

ROYAL SOCIETY OF CHEMISTRY

PAPER
Geunsik Lee, Kwanyong Seo, Tae-Hyuk Kwon *et al.*
Deep metal-assisted chemical etching using a porous monolithic AgAu layer to develop neutral-colored transparent silicon photovoltaics

10 YEARS ANNIVERSARY

See S. Paul, R. Boukherroub, V. Ordomsky *et al.*, *J. Mater. Chem. A*, 2023, **11**, 19338.

ROYAL SOCIETY OF CHEMISTRY

rsc.li/materials-a

Registered charity number: 207890

Journal of
Materials Chemistry A

PAPER

View Article Online
View Journal | View Issue

Check for updates

Cite this: *J. Mater. Chem. A*, 2023, **11**, 19338

Covalent organic framework derived synthesis of Ru embedded in carbon nitride for hydrogen and oxygen evolution reactions†

Tianyu Gao,‡[a] Kilaparthi Sravan Kumar,‡[b] Zhen Yan,[c] Maya Marinova,[d] Martine Trentesaux,[a] Mohammed A. Amin,[e] Sabine Szunerits,[b] Yong Zhou,[a] Vlad Martin-Diaconescu,[f] Sébastien Paul,*[a] Rabah Boukherroub*[b] and Vitaly Ordomsky*[a]

The hydrogen and oxygen evolution reactions (HER and OER) are two steps in electrochemical water splitting for conversion of electric power to chemical energy. The main challenge remains the development of efficient, stable and cheap electrocatalysts able to perform both reactions under alkaline conditions. Single atom Ru stabilized by nitrogen-doped carbon and RuO_2 are currently the materials of choice for the HER and OER, respectively. Here, we propose a strategy for the preparation of Ru embedded in a carbon nitride matrix for efficient HER and OER in KOH solution. It is based on the preparation of a covalent organic framework 2D CIN-1 structure with coordinated Ru^{II}, producing Ru oxide nanoparticles with low valence Ru sites arranged in the form of nanowires between layers of graphitic carbon nitride after pyrolysis. The material demonstrates smaller overpotentials for the HER and OER in comparison with benchmark Pt and RuO_2 catalysts, and high catalytic stability.

Received 5th March 2023
Accepted 6th August 2023

DOI: 10.1039/d3ta01362f

rsc.li/materials-a

1. Introduction

Hydrogen (H_2) is considered as a promising and preferred alternative to fossil fuels due to its high energy density of 120 kJ g^{-1} and eco-friendly emission. Electrocatalytic water splitting, an effective and environmentally friendly technology for H_2 production, has attracted great attention over the last few years[1–4] and is based on the cathodic hydrogen evolution reaction (HER) and anodic oxygen evolution reaction (OER).[5] Noble metal-based catalysts, especially Pt-based catalysts,[6] are at the forefront in boosting the sluggish OER and HER kinetics and remain the benchmark materials for both reactions due to their favorable kinetics for the HER and OER.[7] However, the high cost of Pt metal limits its consideration for commercial and large scale applications for water splitting.

Over the last few decades, a large number of alternative electrocatalysts have been proposed, including non-noble metal and metal-free catalysts.[8–12] Ruthenium is one of the best Pt analogs as it possesses a similar metal hydride (M–H) bond strength of 65 kcal mol^{-1},[13,14] and is more available and five times cheaper than Pt, which makes it popular in catalysis.[15,16] Various scientific reports revealed that the HER performance of Ru is comparable to or even better than that of Pt, in both neutral and alkaline media. Recently, Baek *et al.* synthesized Ru nanoparticles (~2 nm) uniformly dispersed on graphene nanoplatelets (Ru@GnP), and underlined the outstanding HER performance in both acidic and alkaline electrolytes with small overpotentials of 13 mV in 0.5 M H_2SO_4 and 22 mV in 1 M KOH at a current density of 10 mA cm^{-2}.[17] Feng *et al.* reported the electrochemical performance of ruthenium/N-doped carbon (Ru/CN), prepared by electrochemical polymerization of aniline on graphite foam (GF) and dipping the obtained aniline/GF in Ru salt, followed by subsequent pyrolysis of the Ru^{3+}/aniline complex at 900 °C. The resulting material has shown excellent electrocatalytic HER activity with an overpotential of 21 mV (10 mA cm^{-2}) in 1 M KOH.[18] Qiu *et al.* synthesized Ru-based electrocatalysts with abundant Ru active sites using bimetallic MOFs (CuRu-MOF) through pyrolysis and etching of Cu. The as-prepared ultrafine Ru nanoparticles anchored onto hierarchically porous carbon (Ru–HPC) exhibited outstanding HER

---

[a] *Univ. Lille, CNRS, Centrale Lille, ENSCL, Univ. Artois, UMR 8181 – UCCS – Unité de Catalyse et Chimie du Solide, F-59000 Lille, France. E-mail: sebastien.paul@centralelille.fr; vitaly.ordomsky@univ-lille.fr*

[b] *Univ. Lille, CNRS, Univ. Polytechnique Hauts-de-France, UMR 8520 – IEMN, F-59000 Lille, France. E-mail: rabah.boukherroub@univ-lille.fr*

[c] *E2P2L, UMI 3464 CNRS-Solvay, 3966 Jin Du Rd, 201108 Shanghai, China*

[d] *Univ. Lille, CNRS, INRAE, Centrale Lille, Univ. Artois, FR 2638 IMEC Institut Michel-Eugène Chevreul, F-59000 Lille, France*

[e] *Department of Chemistry, College of Science, Taif University, P.O. Box 11099, Taif 21944, Saudi Arabia*

[f] *ALBA Synchrotron – CELLS, Carrer de la Llum 2-26, 08290 Cerdanyola del Vallès, Barcelona, Spain*

† Electronic supplementary information (ESI) available. See DOI: https://doi.org/10.1039/d3ta01362f

‡ These two authors contributed equally to this work.

activity with a low Tafel slope value of 33.9 mV dec^{-1}, even lower than that of commercial 20% Pt/C (41 mV dec^{-1}).[19]

Although recent publications proposed the use of transition metals for the OER,[20] the rutile phase of ruthenium oxide (RuO_2) still serves as a benchmark material for the OER in both acidic and alkaline media.[21,22] The OER activities have been studied for different particle sizes, different crystal structures, and different degrees of hydration and electronic states.[23–25] RuO_2 is limited by its low anodic stability under acidic conditions, especially at high overpotentials as well as by its reduced energy density ($\approx$400 W h kg^{-1}, theoretically), and related low mass activity.[25]

Considering that Ru could be used for both the HER and OER, it would be highly desirable to develop a Ru-based electrocatalyst for efficient water splitting. Ru@RuO_2 core–shell nanorods, synthesized by oxidation of Ru nanorods, indeed demonstrated high efficiency for both the OER and HER reaching overpotentials of 320 and 137 mV, respectively, at a current density of 10 mA cm^{-2}.[26] A possible strategy to improve the electrocatalytic performance would be through the design of catalysts containing highly dispersed Ru stabilized by nitrogen-doped carbon to provide both Ru and RuO_2 at the same time. Ru–N bonding provides several important advantages in comparison with other materials related to the favorable electronic structure of ruthenium, the synergistic effects between Ru and N-doped carbon in reducing water dissociation energy, improved adsorption properties of intermediate reactants and high stability of the Ru species avoiding metal sintering.[27,28]

Recently, solid-state pyrolysis of porous organic networks such as MOFs was widely applied for the facile preparation of metal nanostructures incorporated in porous carbon materials.[29–33] Covalent organic frameworks (COFs) are a new type of microporous materials which are constructed by the covalent linkage of organic building blocks.[34,35] Because of ordered pores, carbon-rich layers and diverse heteroatoms, COFs are promising precursors for the synthesis of carbon-based materials. Surprisingly, they have not been yet used for the preparation of carbon nitrides.

In this work, we synthesized a 2D imine-based COF with an incorporated Ru^{II}–2-diphenylphosphinobenzaldehyde complex. The pyrolysis of this material at 500 °C under a N_2 atmosphere produced highly dispersed RuO_2 nanoparticles containing low valence Ru sites between the layers of carbon nitride. The material provided a high activity for the HER and OER in 1 M KOH.

2. Experimental

2.1. Materials and reagents

$RuCl_3 \cdot H_2O$, 2-(diphenylphosphino)benzaldehyde (DBP), melamine, 1,3,5-triformylbenzene, 1,4-diaminobenzene, 1,4-dioxane and acetic acid were purchased from Sigma-Aldrich. Piperazinedicarbaldehyde, *N*,*N*-dimethylformamide (DMF), dry ethanol, acetone, dichloromethane (CH_2Cl_2) and tetrahydrofuran (THF) were procured from Alfa Aesar. Dimethyl sulfoxide (DMSO) was obtained from Acros Organics.

2.2. Synthesis of materials

2.2.1 Ru–DBP. The tube of a Radleys Carousel reactor was charged with $RuCl_3 \cdot H_2O$ (0.03 g), 2-(diphenylphosphino)benzaldehyde (DBP) (0.03 g) and dimethyl sulfoxide (DMSO, 12 mL). Then, the tube was degassed with dry N_2 and refluxed at 180 °C for 72 h. After that, the precipitated black product was isolated by filtration and washed with dry ethanol, acetone, THF and dichloromethane sequentially. Finally, the product was dried at 100 °C for 48 h to obtain the desired powder Ru–DBP complex.

2.2.2 Ru@CIN-1. The tube of a Radleys Carousel reactor was charged with $RuCl_3 \cdot H_2O$ (0.03 g), 2-(diphenylphosphino) benzaldehyde (0.03 g), piperazinedicarbaldehyde (0.17 g), melamine (0.100 g) and DMSO (12 mL) according to the procedure of CIN-1 material synthesis.[36] The tube was degassed with dry N_2 and refluxed at 180 °C for 72 h in an inert atmosphere. After cooling to room temperature, the precipitated product was isolated by filtration and washed with dry ethanol, acetone, THF and dichloromethane sequentially. Finally, the product was dried at 100 °C for 48 h to obtain the desired powder Ru@CIN-1. Pure CIN-1 was synthesized by the same method without the addition of $RuCl_3 \cdot xH_2O$ and 2-(diphenylphosphino)benzaldehyde.

Ru@CIN-1 and pure CIN-1 were calcined under a N_2 atmosphere at 500 °C for 2 h to yield Ru@g-CN_x and g-CN_x, respectively.

2.3. Characterization

The analysis of Ru and P was performed with the use of an energy dispersive micro X-ray fluorescence spectrometer M4 TORNADO (Bruker). CHNO analysis was performed using a FlashSmart automated analyzer. N, C and H were detected as N_2, CO_2 and H_2O, respectively. The resulting gases were separated on a packed column and detected by using a TCD detector. Oxygen was analyzed separately by pyrolysis with CO analysis.

Fourier transform infrared spectroscopy (FTIR) experiments were carried out with a Thermo Fisher Scientific Nicolet 6700 FTIR instrument (32 scans at a resolution of 4 cm^{-1}) equipped with a mercury cadmium telluride (MCT) detector.

The Raman spectra were recorded on a XploRA Raman confocal microscope from Horiba Jobin Yvon. A 532 nm diode laser was used to excite the samples. The scattered light was guided through a 150 μm pinhole, dispersed and collected using a Peltier-cooled CCD. The laser power was reduced using density filters in order to avoid sample alteration.

The X-ray diffraction patterns (XRD) were recorded on a PANalytical Empyrean X-ray diffractometer in the Bragg–Brentano configuration with a 0.02° step size and 1 s step time. Cu Kα radiation (40 kV and 30 mA) was used as the X-ray source. The interplanar distances were calculated using the Bragg equation: $d = \dfrac{\lambda}{2\sin\theta}$, where λ is the wavelength of X-ray radiation (λ = 1.5406 Å) and θ is the diffraction angle of the peak.

The Brunauer–Emmett–Teller (BET) surface area, pore volume, pore diameter and N_2 sorption–desorption isotherms were measured on a Micromeritics Tristar Model 3020 Surface Area and Porosimetry analyzer. The samples (100 mg) were degassed under vacuum at 250 °C for 2 h prior to N_2 physisorption.

Thermogravimetric analysis (TGA) measurements were performed using an SDT 2960 analyzer from TA Instruments under air flow (50 mL $\min^{-1}$) with a temperature ramping rate of 10 °C $\min^{-1}$.

Scanning transmission electron microscopy (STEM) analysis was performed on a Titan Themis 300 S/TEM equipped with a probe aberration corrector and a monochromator, allowing a special resolution of 70 pm and an energy resolution of 150 meV. The microscope is equipped with a Super-X windowless 4 quadrant SDD (silicon drift detector) detection system for the STEM-energy-dispersive X-ray (EDX) mapping and several annual dark field detectors. The experiment was performed with a spot size of about 500 pm, a semi-convergence angle of 21 mrad, and a probe current of approximately 100 pA. For the high-angle annular dark-field (HAADF) images, the collection angles were between 50 and 200 mrad. The STEM-EDX mapping was acquired with a dwell time of 15 μm per px with continuous scanning over several frames during a total time of 10–15 min per acquisition. The microscope is also equipped with a CETA camera with a 4k × 4k CMOS sensor for the TEM images and diffraction acquisition.

Ru K-edge X-ray absorption spectra (XAS) of samples diluted in cellulose were acquired at room temperature in the form of pellets. XAS spectra were collected in transmission mode for references Ru black, $RuCl_3$ and RuO_2 and fluorescence mode for Ru@ClN-1 and Ru@g-CN_x employing a Si311 double crystal monochromator and a 6 channel multi-element SDD detector available at the CLAESS beamline of the ALBA Synchrotron. Several XAS repeats were collected to ensure reproducibility and statistics. The averaged spectra were treated by using the Athena software package.[37] The energy scale was calibrated by setting the first inflection point of the Ru metal spectra taken as 22 117 eV. EXAFS spectra were extracted using the AUTOBK algorithm employing an R_{bkg} of 1.1 in the 0 to 15.3 Å^{-1} region of k-space. The FEFF6 code[38,39] was used for scattering path generation, and multi (k^1, k^2, k^3)-weighted fits of the data were carried out in r-space and a k-range of 3–14 Å^{-1}. The $S_0{}^2$ value was set to 0.9, and a global E_0 was employed with the initial E_0 value set to the first inflection point of the rising edge. Scattering paths were fit in terms of Δ_{reff} and σ^2, which represent the deviation from the expected interatomic distances and the structural disorder, respectively. To assess the goodness of the fits, both the R_{factor} (% R) and the reduced χ^2 ($\chi_v{}^2$) were minimized, ensuring that the data were not over-fit. An increase in the number of variables is generally expected to improve the R_{factor}; however $\chi_v{}^2$ may go through a minimum and then increase, which is an indication that the model is over-fitting the data.[40] The best fit models were determined using a grid search with fixed values for path coordination numbers by employing Larch, the Python implementation of Artemis.[41]

The X-ray photoelectron spectroscopy (XPS) experiments were carried out using a Kratos Axis Ultra DLD spectrometer, equipped with a monochromatic Al Kα X-ray source (1486.6 eV) operating at 225 W (15 kV, 15 mA). The instrument base pressure was 5×10^{-10} torr and a charge neutralizing system was used for all acquisitions. Analysis was performed at a pass energy of 40 eV and a step size of 0.1 eV. Binding energies (BE) were referenced to the C peak at 285.5 eV.

2.4. Electrochemical methods

The electrocatalytic measurements were performed using a ModuLab-MTS electrochemical test station (Solartron, France) with a conventional three-electrode configuration consisting of a 3 mm diameter glassy carbon (GC) electrode coated with Ru@g-CN_x, a saturated calomel electrode (SCE), $Hg|Hg_2Cl_2$, and Pt coil as the working, reference and counter electrodes, respectively. Before starting the experiments, an aqueous electrolyte solution (1 M KOH) was degassed using nitrogen for at least 30 min. Furthermore, linear sweep voltammetry (LSV) was performed at a scan rate of 5 mV s^{-1} to record the polarization curves.

In order to determine the electrocatalytically active surface area (ECSA), double-layer capacitance (C_{dl}) was calculated by performing cyclic voltammetry (CV) at different scan rates in the non-faradaic potential range (0.11 to 0.24 V *vs.* RHE) of the material. The C_{dl} (μF cm^{-2}) value is determined from the slope of the current density (mA cm^{-2}) as a function of the scan rate (mV s^{-1}) plot. Electrochemical impedance spectroscopy (EIS) was performed at an AC amplitude of 10 mV in a frequency range from 1 kHz to 0.1 Hz at −0.03 V *vs.* RHE. The long-term stability experiments were conducted using the chronopotentiometric technique at a constant current density of −10 mA cm^{-2}. The reference electrode (SHE) was calibrated to the reversible hydrogen electrode (RHE) according to the Nernst equation:

$$E(\text{RHE}) = E(\text{Hg/Hg}_2\text{Cl}_2) + (0.242 + 0.059 \times \text{pH})$$

The pH of the electrolyte solution (1 M KOH) was experimentally determined using a Mettler Toledo pH meter and found to be 13.6 (average of three sets). Hence, we have used this value for calibration during all electrocatalytic experiments. All the electrochemical analyses were conducted without *iR* correction.

In order to prepare the catalyst-modified GC working electrode, 3 mg of the desired catalyst was dispersed in 1 mL of water by ultrasonication for 30 min and then 10 μL of the catalyst suspension was drop-casted onto the GC electrode and dried at 60 °C overnight. Hence, the mass loading on the electrode surface was 0.042 mg cm^{-2}. Furthermore, all the measurements were repeated at least three times to confirm the reproducibility of the material. The turnover frequency (TOF, s^{-1}) measurements were carried out using the formula $Q = \frac{I}{xnF}$, where I is the current (A), x is the number of electrons transferred during the HER (2) and OER (4), F is the Faraday constant (96 485C) and n is the number of active sites calculated by using cyclic voltammograms.[42]

3. Results and discussion

3.1. COF derived synthesis of Ru@g-CN$_x$

A covalent organic framework CIN-1 was synthesized by condensation of piperazinedicarbaldehyde with melamine (Fig. 1). The CHNO analysis revealed the absence of oxygen in CIN-1 with a composition close to the theoretical values (C, 50.5%; N, 44.2%; H, 5.3%) for condensation of an aldehyde with melamine (Table 1). The incorporation of 0.4 wt% of Ru was achieved by the addition of 2-(diphenylphosphino)benzaldehyde as a ligand coordinating with RuCl$_3$ during the crystallization of CIN-1, keeping the composition similar to that of CIN-1.

The pyrolysis of the prepared COF materials by treatment of CIN-1 and Ru@CIN-1 at 500 °C under N$_2$ flow was used to prepare graphitic materials. The chemical analysis of g-CN$_x$ and Ru@g-CN$_x$ revealed a decrease in the hydrogen content and an increase in the contribution of carbon in comparison with that of nitrogen (Table 1), which could be assigned to the partial deamination of the material. The increase in the oxygen content could be ascribed to partial oxidation of the material during contact with air after pyrolysis. The content of Ru in Ru@g-CN$_x$ increased to 0.9 wt% during pyrolysis due to a decrease in the contribution of C, H and N in the material.

X-ray diffraction (XRD) analysis of pure CIN-1 (Fig. 2a) showed only one broad peak at 20° corresponding to the (001) reflection related to interplanar stacking.[43] As reported in the literature, microporous polymers based on Schiff base chemistry are usually amorphous.[44] It is interesting to note that Ru@CIN-1 additionally displayed a sharp peak at 11.9° ascribed to the (100) inplanar structural packing of CIN-1. The increased crystallinity could be assigned to the incorporation of the Ru–DBP complex into the CIN-1 structure which increases the size of the network layer.[45] The XRD patterns of g-CN$_x$ and Ru@g-CN$_x$, after pyrolysis (Fig. 2a), exhibited a distinct shift of the diffraction peak to 26.3° in comparison with those of parent materials; this peak is typical of the (002) diffraction plane for interlayer stacking in graphitic carbon nitrides with a distance between layers of about 0.34 nm, according to the Bragg equation.[46]

As shown in Fig. 2b, the FTIR spectra of pure CIN-1 and Ru@CIN-1 depicted distinct peaks of triazine ring vibrations at 1540, 1490 and 1340 cm^{-1}.[36,47] The FTIR spectrum of the Ru–DBP complex comprised peaks at 1967 cm^{-1} assigned to coordinated C═O stretching vibration, and 1630 and 1400 cm^{-1} due to carbon–carbon stretching vibrations of the aromatic rings.[48] The disappearance of the C═O group vibrations and the appearance of benzene aromatic ring vibrations during the crystallization of Ru@CIN-1 indicated the successful incorporation of the Ru–DBP complex into the CIN-1 structure. FTIR spectra of g-CN$_x$ and Ru@g-CN$_x$ (Fig. 2b) revealed the appearance of bands at 1677 and 1579 cm^{-1}, and a group of peaks in the range of 1250–1500 cm^{-1} ascribed respectively to C═N and aromatic C–N stretching vibrations.[49,50]

Raman spectra of pure CIN-1 and Ru@CIN-1 (Fig. S1, ESI†) confirmed the FTIR results by the presence of characteristic features of the triazine ring (975 cm^{-1}), piperazine ring (1361 & 1429 cm^{-1}) and imine (C═N) stretching vibrations

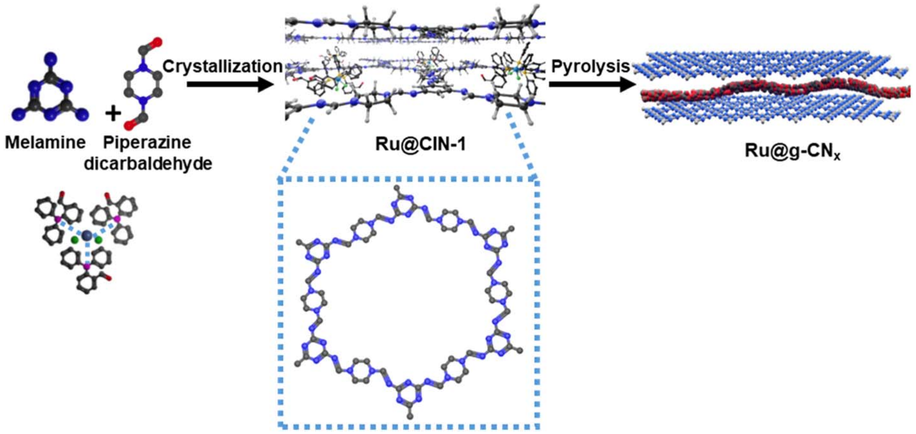

Fig. 1 Schematic illustration of the synthesis of a Ru carbon nitride catalyst.

Table 1 Physical characteristics of CIN-1, g-CN$_x$, Ru@CIN-1 and Ru@g-CN$_x$

Materials	Composition (wt%)						S_{BET} (m^2 g^{-1})	Pore volume (cm^3 g^{-1})
	C	O	N	H	P	Ru		
CIN-1	47.0	—	48.7	4.3	—	—	419.5	0.26
Ru@CIN-1	47.0	0.1	47.5	4.3	0.1	0.4	400.2	0.20
g-CN$_x$	53.0	10.7	33.9	2.4	—	—	61.8	0.21
Ru@g-CN$_x$	39.7	10.9	33.9	2.5	1.2	0.9	23.9	0.18

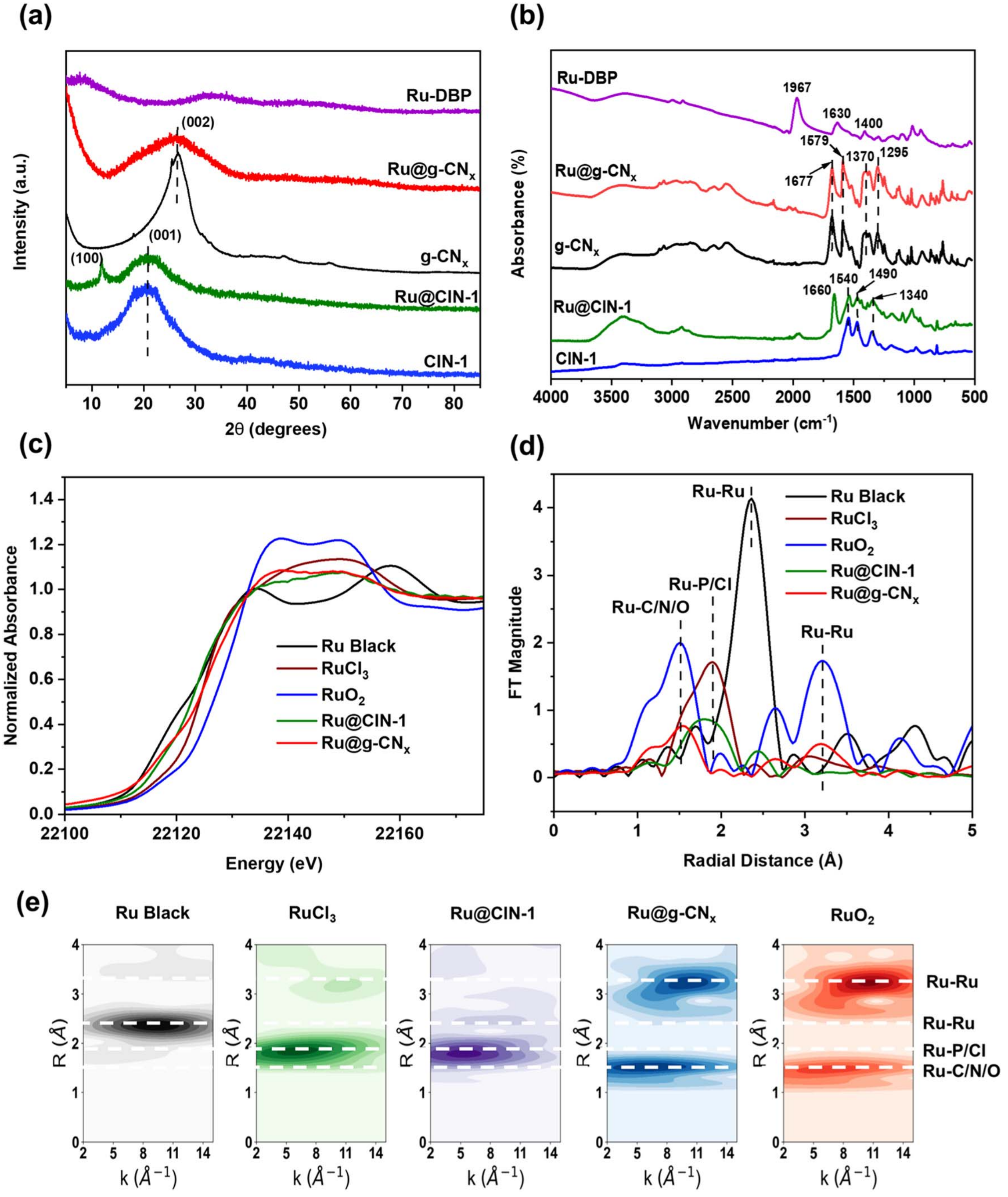

Fig. 2 (a) XRD patterns, (b) FTIR spectra, (c) Ru K-edge XANES spectra, (d) Fourier transformed $\chi(k)$-functions of the EXAFS spectra and (e) Cauchy WT-EXAFS of Ru–DBP, Ru@CIN-1, CIN-1, Ru, RuO$_2$, g-CN$_x$ and Ru@g-CN$_x$.

(1562 cm^{-1}).[47] This differs from the Raman plots of g-CN$_x$ and Ru@g-CN$_x$ which were composed of the characteristic D- and G-bands at around 1357 and 1580 cm^{-1} related to the lattice defects caused by graphite edges with sp^3 bonds of the carbon and graphitic phase containing sp^2 bonds of carbon, respectively.[32,51,52] ^{13}C CP/MAS NMR spectra (Fig. S2, ESI†) also demonstrated the conversion of the peaks corresponding to aliphatic carbon atoms in piperazine at 53.5 ppm and carbon in C=N groups at 166 ppm to a broad asymmetric peak at δ = 150 ppm characteristic of sp^2 aromatic carbons of a graphene sheet after pyrolysis.[53,54]

Transmission electron microscopy (TEM) images revealed a granular morphology of pure CIN-1 with a diameter of particles of about 20 nm in comparison with a layered-sheet structure of imine network layers of 50–200 nm for Ru@CIN-1 (Fig. S3, ESI†). EDX mapping images of the Ru@CIN-1 material confirmed the uniform distribution of Ru and P in the CIN-1 structure (Fig. S4, ESI†). TEM analysis demonstrated that

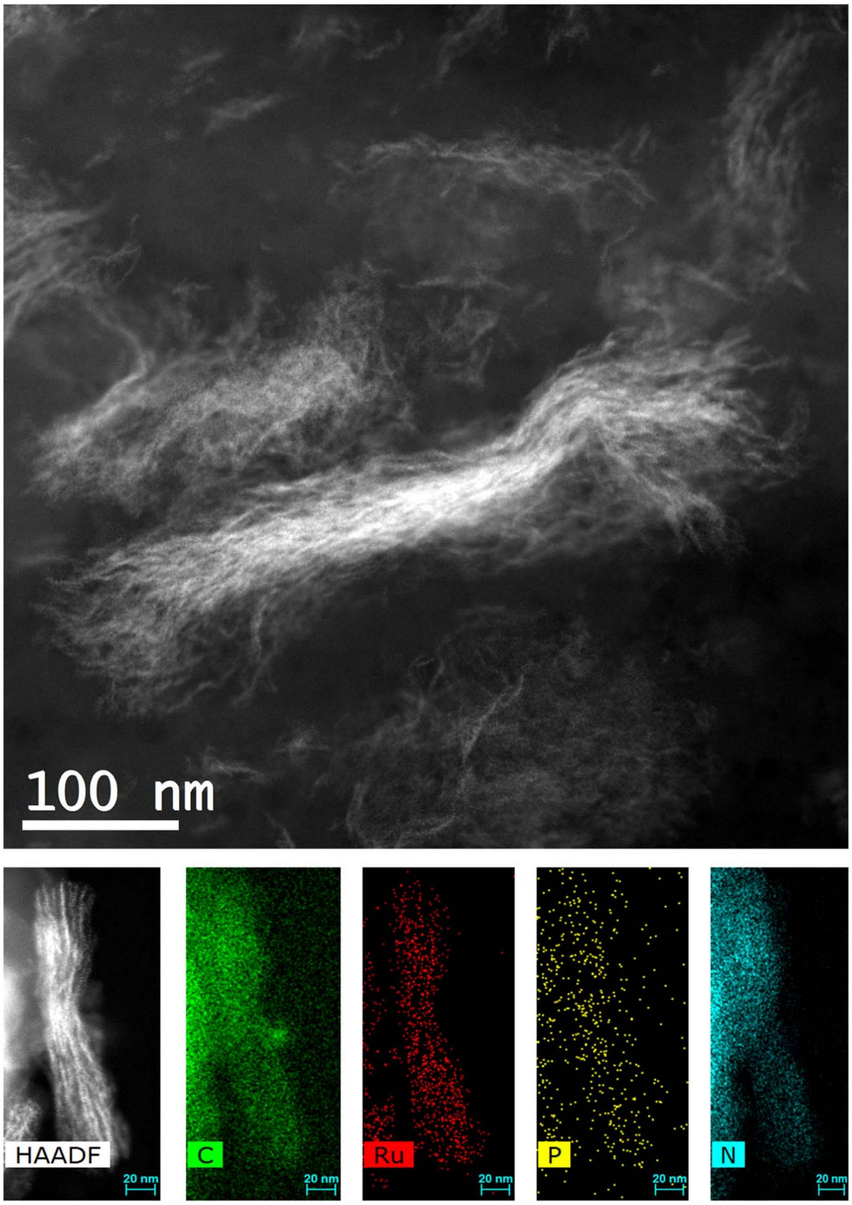

Fig. 3 STEM-HAADF of Ru@g-CN_x with EDX mapping of C, N, P and Ru elements.

pyrolysis resulted in the arrangement of Ru nanoparticles in the form of nanowires between the layers of graphitic carbon nitride for Ru@g-CN_x in comparison with the generation of large carbon nitride particles for g-CN_x material (Fig. 3, S5 and S6, ESI†). These Ru nanowires extend to the size of 500 nm and consist of Ru nanoparticles localized between carbon nitride layers, according to the proposed structure of the initial material (Fig. 1 and S5, ESI†). Elemental mapping demonstrated that Ru, N, P and C are present together in the material and pyrolysis does not affect the distribution of elements.

The CIN-1 and Ru@CIN-1 materials exhibited a type II N_2 adsorption isotherm with a sharp uptake below 0.05 P/P_0, indicating the presence of micropores between the layers and a second uptake at a higher relative pressure originating from the textural pores generated by COF nanoparticles (Fig. S7, ESI†). The Brunauer–Emmett–Teller (BET) surface area values of CIN-1 and Ru@CIN-1 are 419 and 400 $m^2\ g^{-1}$, respectively, which match well with the literature[55] (Table 1). Pyrolysis induced a significant decrease in N_2 adsorption in comparison with the parent materials reaching 62 and 23 $m^2\ g^{-1}$ for g-CN_x and Ru@g-CN_x, respectively, which are usual values for carbon nitride materials[56,57] (Fig. S7, ESI†).

The electronic state of Ru was studied by X-ray absorption spectroscopy (XAS) analysis (Fig. 2c–e, S8 and Table S1, ESI†). The Ru@CIN-1 X-ray absorption near edge structure (XANES) and extended X-ray absorption fine structure (EXAFS) spectra featured a similar profile to that of $RuCl_3$ although the Ru centers are effectively more reduced in Ru@CIN-1 compared to $RuCl_3$. The pyrolysis produced Ru@g-CN_x possessing a spectrum with a shape reminiscent of that of RuO_2, with significantly lower intensity and a broader white line. Similarly, Fourier transform (FT) EXAFS of the Ru@g-CN$_x$ sample showed patterns consistent with the presence of RuO$_2$, with lower intensity, equivalent to ~30% RuO$_2$ character. Furthermore, the intensity ratios of the first coordination shell attributable to Ru–C/N/O at ~1.97 Å in the sample relative to the longer scattering shells in the 3 to 6 Å range of 1.2 : 1 relative to the 1 : 1 found in the RuO$_2$ reference inferred the presence of single Ru centers most probably stabilized by N of carbon nitride (Fig. 2 and Table S1, ESI†). The interaction of Ru with electronegative N in carbon nitride has been ascribed earlier to high dispersion of metals,[58] high stability under working conditions[59] and capture of electrons with optimized adsorption/desorption behaviour in the HER and OER.[28,60,61] Together with the low coordination number, and rising edge energies indicating an average Ru oxidation of +0.5 for Ru@g-CN$_x$, the data are consistent with low valence Ru centers,[62] having a low coordination number together with a RuO$_2$ lattice having O vacancies. XPS Ru 3d analysis confirms the presence of Ru^{2+} in Ru@CIN-1 and Ru–DBP with peaks at 281.4 and 280.9 eV, respectively (Fig. S9, ESI†). Ru@g-CN$_x$ has two doublets with BE Ru 3d$_{5/2}$ 280.7 and 282.4 eV, which can be assigned to RuO$_2$ and Ru(OH)$_3$, respectively.[63]

To conclude, the characterization results demonstrated Ru incorporation in the presence of a triphenylphosphine ligand in the structure of CIN-1 material. Pyrolysis of COF-based materials led to the generation of graphitic carbon nitride materials with RuO$_2$ nanowires containing Ru in a low valence state.

3.2. Electrochemical properties

The performance of the Ru@g-CN$_x$ coated on a GC electrode for the HER in potassium hydroxide (1 M KOH) solution was investigated by performing LSV polarizations at a scan rate of 5 mV s^{-1}. The overpotential *versus* the reversible hydrogen electrode (RHE) at 10 mA cm^{-2}, the anticipated current density for a 12.3% efficient solar water-splitting device, was used to assess the HER performance. Fig. 4a reveals that Ru@g-CN$_x$ had superior electrocatalytic activity by requiring only 53.2 mV for driving a current density of 10 mA cm^{-2}, which is far better than those of RuO$_2$, g-CN$_x$, Ru@CIN-1 and CIN-1. This interface also displayed better catalytic activity than the benchmarked Pt electrode exhibiting an overpotential of 63.7 mV at 10 mA cm^{-2}, comparable to the performance of the most efficient materials reported in the literature[64] (Table S2, ESI†).

The Tafel slope analysis gave us profound insight into the kinetic analysis of the HER derived from the LSV plots usually

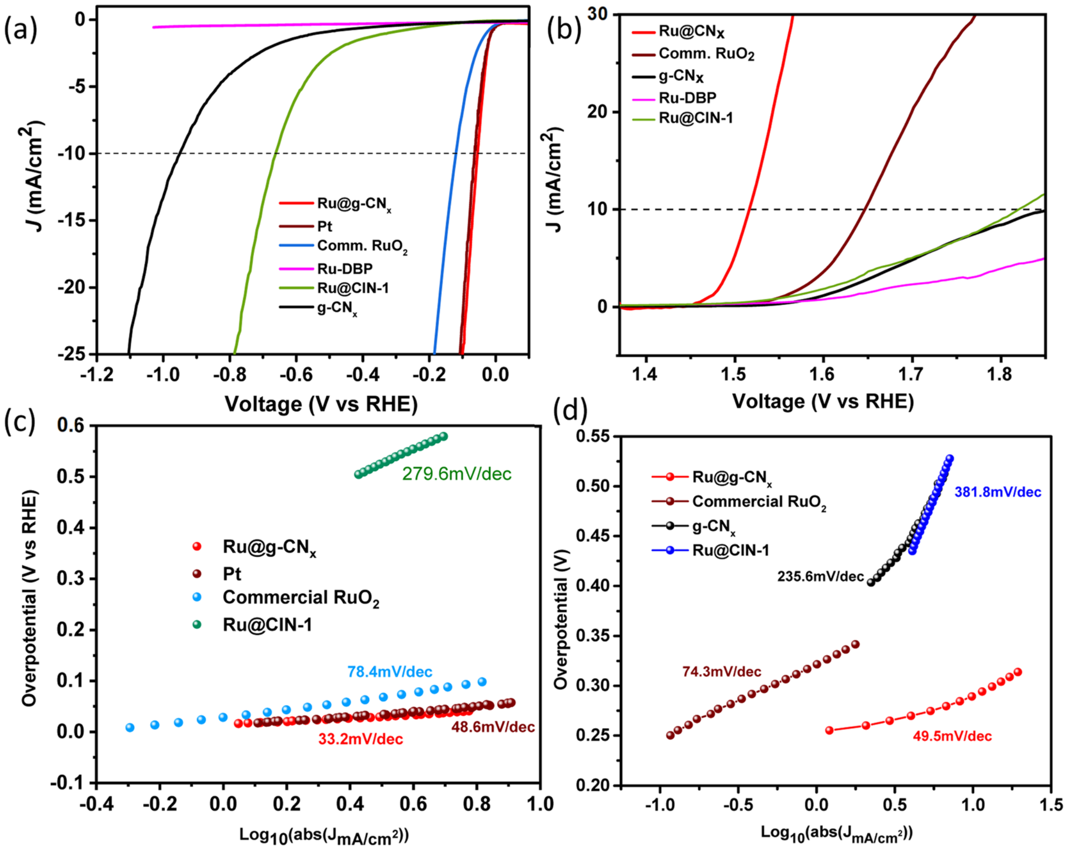

Fig. 4 (a) HER polarization curves of Pt, Ru@g-CN$_x$, commercial RuO$_2$, Ru@CIN-1, Ru–DBP and g-CN$_x$ acquired at a scan rate of 5 mV s^{-1} in 1 M KOH solution. (b) OER polarization curves of commercial RuO$_2$, Ru@g-CN$_x$, Ru@CIN-1 and g-CN$_x$. (c) Tafel plots and slope values of RuO$_2$, Pt, Ru@g-CN$_x$, Ru@CIN-1 and g-CN$_x$ derived from cathodic polarization LSV plots of (a). (d) Tafel plots and slope values of Ru@g-CN$_x$, RuO$_2$, Ru@CIN-1 and g-CN$_x$ derived from anodic polarization LSV plots of (b).

with lower Tafel slopes attributed to faster kinetics. Fig. 4c illustrates the Tafel slope of the Ru@g-CN$_x$ electrode, which is close to 30 mV dec^{-1}, indicating a faster HER rate and Tafel–Volmer mechanism (1, 3) with electrochemical H_2 desorption as the rate-determining step in the HER process. The Tafel slope values of Ru@CIN-1 (279.6 mV dec^{-1}) and RuO_2 (78.4 mV dec^{-1}) were also determined from the LSV curves, which are significantly higher than those of Ru@g-CN$_x$, suggesting that the HER proceeds *via* a primary discharge step.

$$\mathrm{RuO + H_2O + e^- \rightarrow RuOH_{ads} + OH^-}\ \text{(Volmer)} \quad (1)$$

$$\mathrm{RuOH_{ads} + H_2O + e^- \rightarrow RuO + H_2 + OH^-}\ \text{(Heyrovsky)} \quad (2)$$

$$\mathrm{RuOH_{ads} + RuOH_{ads} \rightarrow 2\text{-}RuO + H_2}\ \text{(Tafel)} \quad (3)$$

Furthermore, the oxygen evolution performance of Ru@g-CN$_x$ was assessed in 1.0 M KOH aqueous solution in a three-electrode system. It could be seen from the LSV curves of Ru@g-CN$_x$, RuO_2, Ru@CIN-1 and g-CN$_x$ that oxygen evolution takes place at a much lower overpotential of 280 mV for Ru@g-CN$_x$ at a benchmark current density of 10 mA cm^{-2}, as shown in Fig. 4. The Tafel slope value of Ru@g-CN$_x$ is around 49.5 mV dec^{-1}, lower than that of commercial RuO_2 (74.3 mV dec^{-1}), Ru@CIN-1 (381.8 mV dec^{-1}) and g-CN$_x$ (235.6 mV dec^{-1}), which states that the kinetics of Ru@g-CN$_x$ for the water oxidation reaction follows the Volmer–Heyrovsky reaction pathway (Fig. 4). The Ru@g-CN$_x$ catalyst features a performance comparable to that of the most efficient materials for the OER[65] (Table S3, ESI†).

The result was further supported by the Nyquist plots, showing that Ru@g-CN$_x$ has enhanced electron transfer ability compared to Ru@CIN-1 and g-CN$_x$, as shown in Fig. 5. The three samples exhibited comparable solution resistance (R_s) values, as shown in EIS Nyquist graphs, but different charge transfer resistance (R_{ct}) values. The sequence of HER activity is well supported by the fact that Ru@g-CN$_x$ has the smallest R_{ct} of 45.8 Ω and Ru@CIN-1 and g-CN$_x$ displayed the largest R_{ct} values. The smallest charge transfer implies fast electron transfer to the interface during the HER or OER, which, in turn, guarantees better catalytic activity. LSV measurements of the catalysts were subsequently carried out in the presence of blocking ligands like thiocyanate ions (SCN^-) to identify the HER-active centers

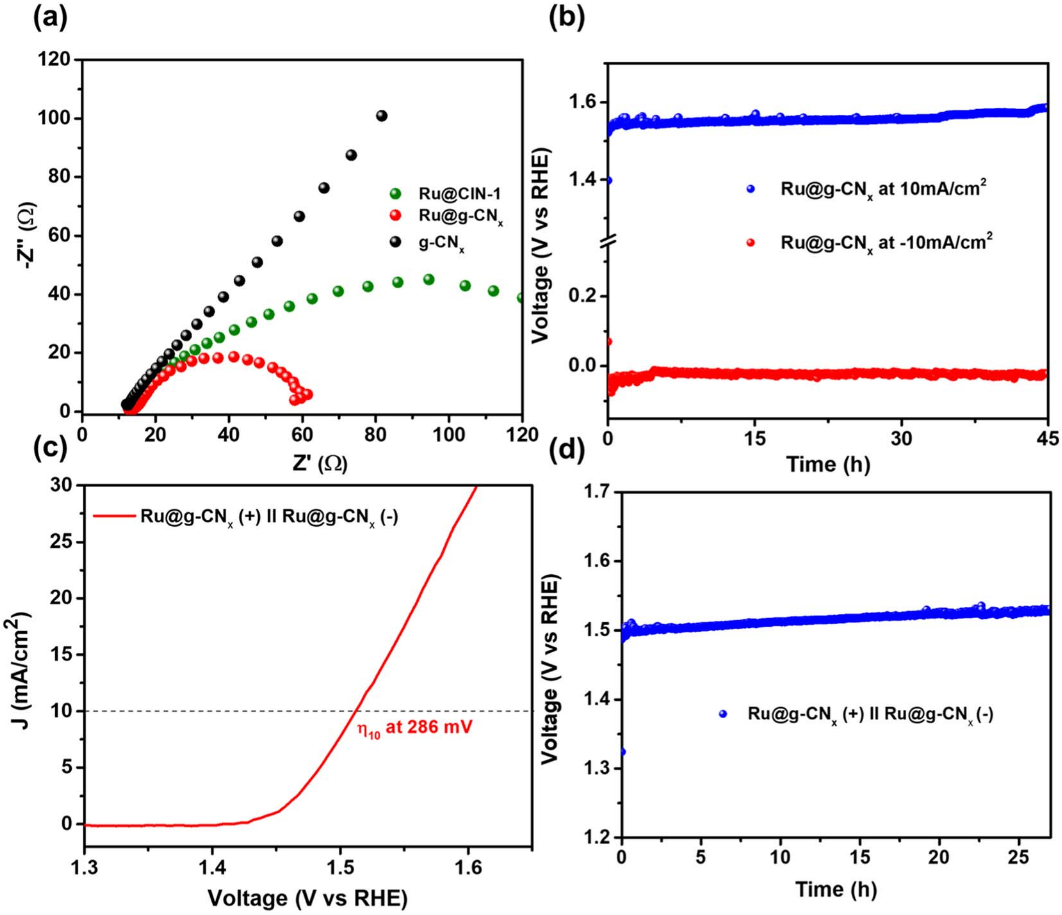

Fig. 5 (a) Nyquist plots of various materials recorded in the range of 1 kHz to 0.1 Hz at a constant potential of 30 mV *vs.* RHE at 10 mV amplitude. (b) Chronopotentiometric plots of Ru@g-CN$_x$ at a current density of 10 mA cm^{-2} and −10 mA cm^{-2} for the OER and HER, respectively in 1 M KOH. (c) LSV plot of overall water splitting in 1 M KOH using Ru@g-CN$_x$ as both the anode and cathode. (d) Chronoamperometric measurements of overall water splitting in 1 M KOH aqueous solution at a constant current density of 10 mA cm^{-2} using Ru@g-CN$_x$ as both the anode and cathode.

of Ru@g-CN$_x$. According to Fig. S10, ESI,† the Ru@g-CN$_x$ electrocatalyst's LSV curve revealed a sharp cathodic shift when SCN$^-$ is present, indicating that Ru particles serve as the active sites.

For the practical application of any catalyst, stability is one of the key factors being judged. The long-term stability of the Ru@g-CN$_x$ catalyst was probed by using potential–time plots in an alkaline environment. The chronopotentiometric plots of the Ru@g-CN$_x$ catalyst obtained in 1.0 M KOH aqueous solution at current densities of −10 mA cm^{-2} and 10 mA cm^{-2} for the HER and OER, respectively, are depicted in Fig. 5. After constant current density for 45 h, a limited decline (about 3%) of the catalyst performance for the OER was registered, while no obvious decrease in performance was observed during the HER stability test. The identical LSV polarization curves of Ru@g-CN$_x$ before and after 10 000 CV cycles for both the HER and OER also confirmed the high stability of the catalyst (Fig. S11, ESI†). This robustness indicates that the catalyst is by far one of the best catalysts reported for water splitting. The analysis of hydrogen and oxygen production showed that Ru@g-CN$_x$ achieved a faradaic efficiency (FE) of almost 100% for actual water splitting, *i.e.* (99.78 and 99.73% for the HER and OER, respectively) (Fig. S12, ESI†). The microscopic analysis of the catalyst after the reaction revealed the presence of Ru in the form of nanowires in the carbon nitride matrix (Fig. S13, ESI†).

It is interesting to note that Ru according to XPS analysis is still in the form of a mixture of RuO_2 and $Ru(OH)_3$ after the OER; however, it is partially reduced to metallic Ru after the HER (Fig. S9, ESI†). The change in the oxidation state to adapt for the target reaction explains high efficiency in both the HER and OER. A variety of 2D or 1D metal nanostructured hydroxides/oxides of transition metals have been used as well for both the HER and OER.[66,67]

In order to understand the enhancement of electrocatalytic activity during the HER and OER for Ru@g-CN$_x$ compared to Ru@CIN-1 and g-CN$_x$, the electrochemical active surface areas (ECSAs) were determined from the electrical double-layer capacitance (C_{dl}). Cyclic voltammograms were measured in a non-faradaic potential region between 0.1 and 0.25 V *vs.* RHE at different scan rates (Fig. S14, ESI†). Theoretically, it is acknowledged that the ECSA is proportional to its C_{dl} value for electrocatalysts with a similar composition.

The C_{dl} values of Ru@g-CN$_x$ (9.1 mF cm^{-2}), g-CN$_x$ (0.25 mF cm^{-2}), and CIN-1 (0.75 mF cm^{-2}) were calculated from the slope of the straight line of the current density *vs.* scan rate curves in Fig. S14, ESI.† Hence, the ECSA experiments revealed that the Ru@g-CN$_x$ catalyst had the highest number of active sites caused by the lattice defects. This explains the catalytic behavior of the catalyst. The ECSA-normalized LSV curves for both the HER and OER were plotted to understand the intrinsic catalytic activity of the samples. In Fig. S15, ESI† we see that in both the HER and OER, Ru@g-CN$_x$ has higher catalytic activity than the precursor compounds. We have further employed per-site turnover frequency (TOF) analysis to compare the practical performance of the catalysts. The TOF curves, which vary with potential, revealed a higher intrinsic activity per site in the Ru@g-CN$_x$ catalyst when compared to both the Ru@CIN-1 and g-CN$_x$ catalysts (Fig. S15, ESI†).

Due to the robust catalytic activity of Ru@g-CN$_x$, we were motivated to perform the overall water splitting in a 2-electrode system at 10 mA cm^{-2} for 26 h, as shown in Fig. 5. The LSV plot of the system recorded an overpotential of just 286 mV *vs.* RHE at a scan rate of 5 mV s^{-1}. The chronopotentiometric plot showed that the catalyst had a good performance at a constant supply of 10 mA cm^{-2} in 1 M KOH electrolyte solution with a limited degradation of 1.35% after 26 h. The electrolyzer only required a cell voltage of 1.51 V to generate a current density of 10 mA cm^{-2}, which is quite outstanding and comparable to that of the newly reported state-of-the-art materials for total water splitting (Table S4, ESI†).

4. Conclusion

In summary, we demonstrated the synthesis of a novel functional Ru electrocatalyst embedded in graphite carbon nitride prepared by pyrolysis of a covalent organic framework incorporated Ru complex. This resulted in the generation of Ru oxide nanowires with a low valence state of Ru between the layers of graphitic carbon nitride after pyrolysis. The resulting material exhibited a very low overpotential of just 53.2 mV to achieve a current density of 10 mA cm^{-2} and a Tafel slope of 33.2 mV dec^{-1} for the HER in an alkaline medium (1 M KOH). In addition, the catalyst performed very well during the OER with an overpotential of only 280 mV at 10 mA cm^{-2} and a low Tafel slope of 49.5 mV dec^{-1}, exceeding the performance of commercially available RuO_2. The improved catalytic activity was attributed to the generation of a large number of active sites, as witnessed by electrochemical active surface area and charge transfer resistance results from EIS. Furthermore, chronopotentiometry measurements concluded that the catalyst is highly stable in a corrosion-free environment for at least 45 h producing both hydrogen and oxygen. Furthermore, the robustness of the developed electrocatalyst was demonstrated in a full water splitting configuration with a slight degradation of 1.35% for at least 26 h for delivering a current density of 10 mA cm^{-2}.

Data availability

All data generated or analysed during this study are included in this published article (and its ESI file†).

Conflicts of interest

The authors declare that they have no competing interests.

Acknowledgements

The authors thank Solvay for the financial support of this work. The Chevreul Institute is thanked for its help in the development of this work through the ARCHICM project supported by the “Ministère de l'Enseignement Supérieur de la Recherche et de l'Innovation”, the region “Hauts-de-France”, the ERDF program of the European Union and the "Métropole Européenne de Lille" and the CPER "Wavetech". The authors would like to thank Mr Florent Blanchard and Mr Ahmed Addad for their help in carrying out the work on the X-ray diffraction and electron microscopy facilities of the Advanced Characterization Platform of the Chevreul Institute. The authors also thank Mr Olivier Gardoll and Mrs Joelle Thuriot for their help in TGA and XRF. Tianyu Gao thanks the China Scholarship Council (CSC No. 201807030012) for the financial support. K. Sravan also acknowledges financial support from the Hauts-de-France region and CEFIPRA. The authors are also thankful to the Taif University Researchers Supporting Project number (TURSP-2020/03), Taif University, Taif, Saudi Arabia. XAS experiments were performed at the BL22-CLAESS beamline at ALBA Synchrotron with the collaboration of ALBA staff as part of projects 2022035778 and 2022035785.

References

1 H. Ishaq, I. Dincer and C. Crawford, *Int. J. Hydrogen Energy*, 2022, **47**, 26238–26264.

2 P. J. Megía, A. J. Vizcaíno, J. A. Calles and A. Carrero, *Energy Fuels*, 2021, **35**, 16403–16415.

3 L. Schlapbach and A. Züttel, *Nature*, 2001, **414**, 353–358.

4 J. A. Turner, *Science*, 2004, **305**, 972–974.

5 W. Zhou, J. Jia, J. Lu, L. Yang, D. Hou, G. Li and S. Chen, *Nano Energy*, 2016, **28**, 29–43.

6 M. F. Neira D'Angelo, V. Ordomsky, J. van der Schaaf, J. C. Schouten and T. A. Nijhuis, *Catal. Sci. Technol.*, 2013, **3**, 2834–2842.

7 M. Carmo, D. L. Fritz, J. Mergel and D. Stolten, *Int. J. Hydrogen Energy*, 2013, **38**, 4901–4934.

8 S. H. Ahn, S. J. Hwang, S. J. Yoo, I. Choi, H.-J. Kim, J. H. Jang, S. W. Nam, T.-H. Lim, T. Lim, S.-K. Kim and J. J. Kim, *J. Mater. Chem.*, 2012, **22**, 15153–15159.

9 X. Wen, X. Yang, M. Li, L. Bai and J. Guan, *Electrochim. Acta*, 2018, **296**, 830–841.

10 A. Phuruangrat, D. J. Ham, S. J. Hong, S. Thongtem and J. S. Lee, *J. Mater. Chem.*, 2010, **20**, 1683–1690.

11 R. Subbaraman, D. Tripkovic, K.-C. Chang, D. Strmcnik, A. P. Paulikas, P. Hirunsit, M. Chan, J. Greeley, V. Stamenkovic and N. M. Markovic, *Nat. Mater.*, 2012, **11**, 550–557.

12 W.-J. Jiang, S. Niu, T. Tang, Q.-H. Zhang, X.-Z. Liu, Y. Zhang, Y.-Y. Chen, J.-H. Li, L. Gu, L.-J. Wan and J.-S. Hu, *Angew. Chem., Int. Ed.*, 2017, **56**, 6572–6577.

13 S. Cherevko, S. Geiger, O. Kasian, N. Kulyk, J.-P. Grote, A. Savan, B. R. Shrestha, S. Merzlikin, B. Breitbach, A. Ludwig and K. J. J. Mayrhofer, *Catal. Today*, 2016, **262**, 170–180.

14 B. Sarkar, D. Das and K. K. Nanda, *J. Mater. Chem. A*, 2021, **9**, 13958–13966.

15 Q. Wang, S. Santos, C. A. Urbina-Blanco, W. Y. Hernández, M. Impéror-Clerc, E. I. Vovk, M. Marinova, O. Ersen, W. Baaziz, O. V. Safonova, A. Y. Khodakov, M. Saeys and V. V. Ordomsky, *Appl. Catal., B*, 2021, **290**, 120036.

16 D. Wu, Q. Wang, O. V. Safonova, D. V. Peron, W. Zhou, Z. Yan, M. Marinova, A. Y. Khodakov and V. V. Ordomsky, *Angew. Chem., Int. Ed.*, 2021, **60**, 12513–12523.

17 F. Li, G.-F. Han, H.-J. Noh, I. Ahmad, I.-Y. Jeon and J.-B. Baek, *Adv. Mater.*, 2018, **30**, 1803676.

18 J. Zhang, P. Liu, G. Wang, P. P. Zhang, X. D. Zhuang, M. W. Chen, I. M. Weidinger and X. L. Feng, *J. Mater. Chem. A*, 2017, **5**, 25314–25318.

19 T. Qiu, Z. Liang, W. Guo, S. Gao, C. Qu, H. Tabassum, H. Zhang, B. Zhu, R. Zou and Y. Shao-Horn, *Nano Energy*, 2019, **58**, 1–10.

20 Y. Wang, L. Zhao, J. Ma and J. Zhang, *Energy Environ. Sci.*, 2022, **15**, 3830–3841.

21 H. Sun and W. Jung, *J. Mater. Chem. A*, 2021, **9**, 15506–15521.

22 J. Song, C. Wei, Z.-F. Huang, C. Liu, L. Zeng, X. Wang and Z. J. Xu, *Chem. Soc. Rev.*, 2020, **49**, 2196–2214.

23 E. Tsuji, A. Imanishi, K.-i. Fukui and Y. Nakato, *Electrochim. Acta*, 2011, **56**, 2009–2016.

24 K. Biswas and C. N. Rao, *J. Nanosci. Nanotechnol.*, 2007, **7**, 1969–1974.

25 Y. Qin, T. Yu, S. Deng, X.-Y. Zhou, D. Lin, Q. Zhang, Z. Jin, D. Zhang, Y.-B. He, H.-J. Qiu, L. He, F. Kang, K. Li and T.-Y. Zhang, *Nat. Commun.*, 2022, **13**, 3784.

26 R. Jiang, D. T. Tran, J. Li and D. Chu, *Energy Environ. Mater.*, 2019, **2**, 201–208.

27 J. Wang, X. Guan, H. Li, S. Zeng, R. Li, Q. Yao, H. Chen, Y. Zheng and K. Qu, *Nano Energy*, 2022, **100**, 107467.

28 X. Gao, J. Chen, X. Sun, B. Wu, B. Li, Z. Ning, J. Li and N. Wang, *ACS Appl. Nano Mater.*, 2020, **3**, 12269–12277.

29 G. Kim, J. Yang, N. Nakashima and T. Shiraki, *Chem.–Eur. J.*, 2017, **23**, 17504–17510.

30 L. Chen, L. Zhang, Z. Chen, H. Liu, R. Luque and Y. Li, *Chem. Sci.*, 2016, **7**, 6015–6020.

31 Q. Xu, Y. Tang, L. Zhai, Q. Chen and D. Jiang, *Chem. Commun.*, 2017, **53**, 11690–11693.

32 X. Hu, Y. Long, M. Fan, M. Yuan, H. Zhao, J. Ma and Z. Dong, *Appl. Catal., B*, 2019, **244**, 25–35.

33 Q. Xu, Y. Tang, X. Zhang, Y. Oshima, Q. Chen and D. Jiang, *Adv. Mater.*, 2018, **30**, e1706330.

34 S. Y. Ding and W. Wang, *Chem. Soc. Rev.*, 2013, **42**, 548–568.

35 P. J. Waller, F. Gandara and O. M. Yaghi, *Acc. Chem. Res.*, 2015, **48**, 3053–3063.

36 T. Gao, Z. Yan, V. Ordomsky and S. Paul, *ChemCatChem*, 2022, **14**, e202101450.

37 B. Ravel and M. Newville, *J. Synchrotron Radiat.*, 2005, **12**, 537–541.

38 M. Newville, *J. Synchrotron Radiat.*, 2001, **8**, 96–100.

39 J. J. Rehr and R. C. Albers, *Rev. Mod. Phys.*, 2000, **72**, 621–654.

40 P. R. Bevington and D. K. Robinson, *Data Reduction and Error Analysis for the Physical Sciences*, McGraw-Hill, New York, 2nd edn, 1992.

41 M. Newville, *J. Phys.: Conf. Ser.*, 2013, **430**, 1–7.

42 Y.-R. Liu, X. Shang, W.-K. Gao, B. Dong, J.-Q. Chi, X. Li, K.-L. Yan, Y.-M. Chai, Y.-Q. Liu and C.-G. Liu, *Appl. Surf. Sci.*, 2017, **412**, 138–145.

43 S.-Y. Li, W.-H. Li, X.-L. Wu, Y. Tian, J. Yue and G. Zhu, *Chem. Sci.*, 2019, **10**, 7695–7701.

44 M. G. Schwab, B. Fassbender, H. W. Spiess, A. Thomas, X. Feng and K. Müllen, *J. Am. Chem. Soc.*, 2009, **131**, 7216–7217.

45 S. Roy, T. Chatterjee, B. Banerjee, N. Salam, A. Bhaumik and S. M. Islam, *RSC Adv.*, 2014, **4**, 46075–46083.

46 J. Liu, Y. Zhang, L. Zhang, F. Xie, A. Vasileff and S.-Z. Qiao, *Adv. Mater.*, 2019, **31**, 1901261.

47 J. Xue, Y. Bai and H. Liu, *Anal. Bioanal. Chem.*, 2019, **411**, 3721–3729.

48 J. G. Małecki and A. Maroń, *Transition Met. Chem.*, 2012, **37**, 727–734.

49 N. Bandara, Y. Esparza and J. Wu, *Sci. Rep.*, 2017, **7**, 11538.

50 M. P. Kumar, T. Kesavan, G. Kalita, P. Ragupathy, T. N. Narayanan and D. K. Pattanayak, *RSC Adv.*, 2014, **4**, 38689–38697.

51 Y. Zhang, Y. Ma, Y.-Y. Chen, L. Zhao, L.-B. Huang, H. Luo, W.-J. Jiang, X. Zhang, S. Niu, D. Gao, J. Bi, G. Fan and J.-S. Hu, *ACS Appl. Mater. Interfaces*, 2017, **9**, 36857–36864.

52 X. Cui, Y. Long, X. Zhou, G. Yu, J. Yang, M. Yuan, J. Ma and Z. Dong, *Green Chem.*, 2018, **20**, 1121–1130.

53 H. Darmstadt, C. Roy, S. Kaliaguine, G. Xu, M. Auger, A. Tuel and V. Ramaswamy, *Carbon*, 2000, **38**, 1279–1287.

54 A. M. Panich, A. I. Shames and N. A. Sergeev, *Appl. Magn. Reson.*, 2013, **44**, 107–116.

55 M. K. Bhunia, S. K. Das, P. Pachfule, R. Banerjee and A. Bhaumik, *Dalton Trans.*, 2012, **41**, 1304–1311.

56 E. Alwin, M. Zieliński, A. Suchora, I. Gulaczyk, Z. Piskuła and M. Pietrowski, *J. Mater. Sci.*, 2022, **57**, 15705–15721.

57 H. Wang, X. Yuan, Y. Wu, G. Zeng, X. Chen, L. Leng and H. Li, *Appl. Catal., B*, 2015, **174–175**, 445–454.

58 Z. Yu, Y. Li, A. Torres-Pinto, A. P. LaGrow, V. M. Diaconescu, L. Simonelli, M. J. Sampaio, O. Bondarchuk, I. Amorim, A. Araujo, A. M. T. Silva, C. G. Silva, J. L. Faria and L. Liu, *Appl. Catal., B*, 2022, **310**, 121318.

59 X. Zhang, Z. Xia, H. Li, S. Yu, S. Wang and G. Sun, *J. Colloid Interface Sci.*, 2023, **640**, 170–178.

60 B. Jiang, Z. Wang, L. Cheng, Z. Chen, Y. Dong, X. Wang, T. Wang, X. Mao, Y. Gao, Z. Xu, K. Yin and K. Wu, *J. Alloys Compd.*, 2023, **939**, 168717.

61 M. Gao, Z. Wang, S. Sun, D. Jiang, W. Wei and M. Chen, *J. Alloys Compd.*, 2021, **864**, 158174.

62 F. J. Escobar-Bedia, M. Lopez-Haro, J. J. Calvino, V. Martin-Diaconescu, L. Simonelli, V. Perez-Dieste, M. J. Sabater, P. Concepción and A. Corma, *ACS Catal.*, 2022, **12**, 4182–4193.

63 D. J. Morgan, *Surf. Interface Anal.*, 2015, **47**, 1072–1079.

64 J. Ding, Q. Shao, Y. Feng and X. Huang, *Nano Energy*, 2018, **47**, 1–7.

65 C.-Z. Yuan, Y.-F. Jiang, Z.-W. Zhao, S.-J. Zhao, X. Zhou, T.-Y. Cheang and A.-W. Xu, *ACS Sustainable Chem. Eng.*, 2018, **6**, 11529–11535.

66 Y. Wang, J. Ma, J. Wang, S. Chen, H. Wang and J. Zhang, *Adv. Energy Mater.*, 2019, **9**, 1802939.

67 Y. Wang, S. Chen and J. Zhang, *Adv. Funct. Mater.*, 2019, **29**, 1904955.